Journal of
Applied
Crystallography

ISSN 1600-5767

Received 11 December 2013
Accepted 16 June 2014

Comparison between a near-field and a far-field indexing approach for characterization of a polycrystalline sample volume containing more than 1500 grains

Laura Nervo,[a,b]* Andrew King,[c] Jonathan P. Wright,[a] Wolfgang Ludwig,[d,a] Péter Reischig,[d,e] Joao Quinta da Fonseca[b] and Michael Preuss[b]

[a]European Synchrotron Radiation Facility, 6 Rue Jules Horowitz, BP 220, Grenoble 38043, France, [b]Materials Science Centre, School of Materials, University of Manchester, Oxford Road, Manchester M13 9PL, UK, [c]Synchrotron SOLEIL, L'Orme des Merisiers Saint-Aubin, BP 48, Gif-sur-Yvette 91192, France, [d]MATEIS, INSA de Lyon, Université de Lyon, 7 Avenue Jean Capelle, Villeurbanne 69621, France, and [e]Department of Materials Science and Engineering, Faculty of Mechanical, Maritime and Materials Engineering, Delft University of Technology, Mekelweg 2, Delft 2628 CD, The Netherlands. Correspondence e-mail: laura.nervo@esrf.fr

A comparison of the performance of X-ray diffraction tomography, a near-field diffraction technique, and a far-field diffraction technique for indexing X-ray diffraction data of polycrystalline materials has been carried out by acquiring two sets of diffraction data from the same polycrystalline sample volume. Both approaches used in this study are variants of the three-dimensional X-ray diffraction (3DXRD) methodology, but they rely on different data-collection and analysis strategies. Previous attempts to assess the quality of 3DXRD indexing results from polycrystalline materials have been restricted to comparisons with two-dimensional electron backscatter diffraction cross sections containing a limited number of grains. In the current work, the relative performance of two frequently used polycrystalline-material indexing algorithms is assessed, comparing the indexing results obtained from a three-dimensional sample volume containing more than 1500 grains. The currently achievable accuracy of three-dimensional grain maps produced with these algorithms has been assessed using a statistical analysis of the measurement of the size, position and orientation of the grains in the sample. The material used for this comparison was a polycrystalline commercially pure titanium grade 2 sample, which has a hexagonal close-packed crystal structure. The comparison of the two techniques shows good agreement for the measurements of the grain position, size and orientation. Cross-validation between the indexing results shows that about 99% of the sample volume has been indexed correctly by either of these indexing approaches. The remaining discrepancies have been analysed and the strengths and limitations of both approaches are discussed.

1. Introduction

Over the past ten years, considerable effort has been put into the development of novel three-dimensional diffraction techniques for mapping grain structures in polycrystalline materials. There are two main sets of techniques that aim at a real-space description of polycrystalline materials in terms of the three-dimensional shapes and orientations of all the grains present in the illuminated sample volume.

The first set of techniques are point scanning techniques like diffraction tomography (Stock, 2008; Bleuet *et al.*, 2009) or the polychromatic Laue micro-diffraction technique and its extension into three dimensions *via* differential aperture X-ray microscopy (Larson *et al.*, 2002), where three-dimensional information is obtained by scanning the sample and an analyser wire relative to a point-focused beam. Three-dimensional grain maps produced by this first type of three-dimensional scanning technique offer access to local orientation, phase and strain information, but are typically restricted to small sample volumes because of limitations in scan speed.

The second set of techniques are variants of the monochromatic beam rotating-crystal method, typified by three-dimensional X-ray diffraction (3DXRD) microscopy (Poulsen, 2012; Oddershede *et al.*, 2010, 2012; Sørensen *et al.*, 2012) or high-energy diffraction microscopy (Li *et al.*, 2012).

3DXRD produces three-dimensional maps of the grains, visualizing their position, orientation and elastic strain at the same time, using an extended beam of monochromatic radiation. 3DXRD experiments can be further sub-divided into near- and far-field approaches or combinations of both. Near-field diffraction imaging techniques aim to resolve three-dimensional grain shapes (Suter *et al.*, 2006; Ludwig, King *et al.*, 2009; Schmidt, 2010; Li & Suter, 2013; Reischig *et al.*, 2013) and employ high-resolution X-ray imaging detectors with pixels smaller than the grain size. Far-field approaches, on the other hand, employ a low-resolution detector with pixels comparable to or larger than the grain size, in which case the morphology of the grains is neglected.

The term 3DXRD has in the past been used for both near- and far-field diffraction experiments, and sometimes both detector configurations are used simultaneously. We will use the term 'conventional 3DXRD' to refer to the more frequently used far-field 3DXRD acquisition geometry.

One of the main differences between the near- and far-field acquisition geometries is that, in the near-field configuration, spatial and angular information are mixed and scattering vectors cannot be derived directly from the measurement of the position of a diffraction spot on the detector. Near-field indexing approaches are therefore typically based on one of the following principles, resolving the ambiguity arising from the unknown grain centre-of-mass position: (i) voxel-wise forward modelling (Suter *et al.*, 2006), (ii) ray tracing over several detector positions (Lauridsen *et al.*, 2001) or (iii) identification of Friedel pairs (Ludwig, Reischig *et al.*, 2009).

Indexing from far-field diffraction data can be based on the same three principles, but in many practical cases approximate grain orientations can be identified using scattering vectors derived directly from diffraction spot positions (neglecting the precession of the grain around the axis of rotation). Both grain position and orientation are then refined in a subsequent processing step.

Given the complexity of diffraction patterns arising from sample volumes containing 1000 grains or more, the precision or validity of indexing results obtained by any of the above-mentioned approaches is not trivial to evaluate from a single experiment. The aim of the current study is to compare and cross-validate indexing results obtained from two variants of 3DXRD frequently used on beamline ID11 of the European Synchrotron Radiation Facility (ESRF): (i) X-ray diffraction contrast tomography (DCT) as an instance of a near-field method, and (ii) conventional 3DXRD as a representative of the far-field diffraction method. The data were analysed using the *DCT* code (http://sourceforge.net/projects/dct/) and *ImageD11* software (http://sourceforge.net/projects/fable/), respectively. In §2 we describe the sample preparation and experimental setup and briefly recall the principle of the polycrystalline-material indexing algorithms used in this study. We then proceed with a quantitative analysis and cross-validation of the indexing results obtained with the two approaches (§3). In §4 we discuss the strengths and limitations of both approaches and analyse in more detail the discrepancies observed in the experimental results.

2. Experimental procedure

2.1. Sample preparation and mounting

The experiments were performed on a cylindrical sample of commercially pure titanium (CP-Ti) with an average grain size of 40.5 μm, as determined by electron backscatter diffraction (EBSD). The material was thermomechanically processed and recrystallized at 923 K for 3 h in an argon atmosphere in order to produce grains with a low intragranular orientation spread, and subsquently cooled at a rate of 1 K min^{-1}. A sample with a diameter of 700 μm was cut by electro-discharge machining, with the cylinder axis parallel to the original rolling direction (RD). The cylindrical sample was placed in a small loading rig, with an external compressive load of 15 N along the sample and rotation axis, equivalent to 39 MPa of average normal stress across the cross section. As the yield strength of CP-Ti grade 2 is about one order of magnitude higher than the applied stress (Welsch *et al.*, 1994; Holt *et al.*, 1996), the sample was only deformed elastically. The compression device was designed to suit the space constraints of the near-field acquisition geometry, with typical sample-to-detector distances in the range 3–10 mm. It also allows irradiation of the entire gauge volume during a 360° rotation.

2.2. Experimental setup

The experiment was performed on beamline ID11 of the ESRF (Vaughan *et al.*, 2010) using a monochromatic beam produced by a bent Si(111) Laue–Laue double-crystal monochromator (40 keV, relative energy bandwidth $\Delta\lambda/\lambda \simeq 10^{-3}$). The experimental setup is represented schematically in Fig. 1. The coordinate system is defined such that the X-ray beam is along the laboratory x direction [100], the z direction is vertical, upwards from the origin [001], and the y direction [010] is consistent with a right-handed system. The rotation axis of the sample is right handed and parallel to the z axis. The sample coordinate system rotates around the z axis and it coincides with the laboratory coordinate system when the rotation angle $\omega = 0$. A compression rig hosting the cylinder-shaped sample was mounted on the rotation stage such that the sample and the loading axis were aligned with the rotation axis. The near- and far-field acquisitions were carried out consecutively, without changing the sample mounting or the beam-defining slit settings.

Two FReLoN CCD cameras (Labiche *et al.*, 2007) were used for this experiment, positioned normal to the incident beam, downstream from the sample. Both CCD cameras have an array of 2048 × 2048 pixels. The first is coupled *via* visible light microscope optics to a transparent luminescent screen, giving an effective pixel size of 1.4 μm and a field of view of 2.87 × 2.87 mm. This detector, used for the near-field approach, was placed at a sample-to-detector distance of 7 mm and will be referred to as the near-field detector. In all, 7200 images were recorded during a 360° rotation of the sample, with an exposure time of 1 s, giving a total scan duration of 2.5 h.

The second CCD camera has a fibre-optic coupling (Coan *et al.*, 2006), which gives an effective pixel size of 48.5 μm and a

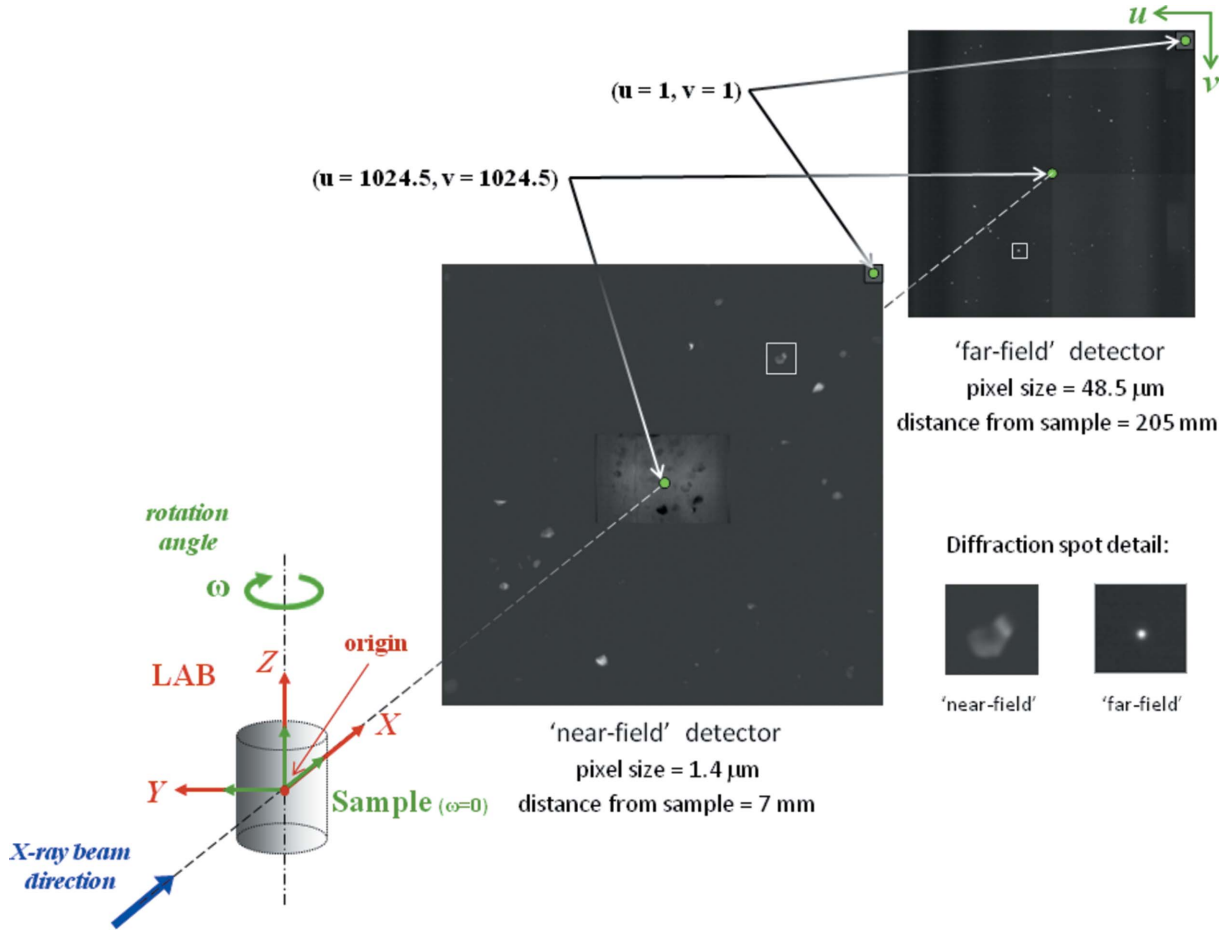

Figure 1
The experimental setup, with high-resolution near-field and low-resolution far-field detectors and a vertical rotation axis configuration, at beamline ID11 of the ESRF (Grenoble, France).

field of view of 99.3 × 99.3 mm. It was placed 205 mm from the sample and was used for the acquisition of far-field diffraction data. In all, 7200 images were recorded during a 360° rotation of the sample, with an exposure time of 0.1 s, giving a total scan duration of 27 min.

The far-field detector cannot spatially resolve grain shape, owing to its larger pixel size and working distance. However, this configuration has a reduced sensitivity to unwanted translational drifts of the setup, leading to more accurate observations of diffraction angle. The large effective pixel size also means that we can use a thicker scintillator screen without degrading the resolution. Consequently, this detector has a higher sensitivity than the near-field detector; hence the counting times are one or two orders of magnitude shorter, and it is generally believed that smaller grains can be detected.

2.3. Data analysis

The data analysis of the near- and far-field diffraction data was carried out using two different software packages. In both cases the data processing involves some basic steps, like determination (fitting) of the global experimental parameters (in particular detector position and tilts), correction of spatial distortions of the detector system and background correction, which are followed by segmentation of connected pixel neighbourhoods (peak search) of the recorded diffraction spots.

Generally speaking, the task of indexing diffraction data from polycrystalline materials corresponds to assigning scattering vectors to grains of origin. In the case of far-field diffraction data, the scattering vectors can, to a first approximation, be derived from the diffraction spot positions, whereas in the case of near-field data an intermediate processing step is required, because of the coupling of spatial and angular information in the diffraction spot centre-of-mass positions. In the case of the near-field data, which were analysed using the *DCT* code, the latter problem is solved by exploiting the symmetry of Friedel pairs (see §4.1 for more details on this aspect). An automated matching procedure working on diffraction spot metadata (*i.e.* spot position, aspect ratio, size and intensity) identifies Friedel pairs of diffraction spots observed at a 180° offset in the sample rotation. Each Friedel pair defines a (diffracted) beam trajectory through the sample volume, from which the direction of the scattering vector can be derived. The actual indexing routine carries out a systematic search among these spot pairs and tries to identify mutually consistent groups of pairs, using a combination of real-space (proximity of beam trajectories in real space) and

crystallographic constraints (valid interplanar angles). Grains with at least five assigned pairs (out of 40 expected) were accepted in the current study. For materials with negligible intragranular orientation spread, the diffraction spots assigned to a grain can be treated as an approximation of parallel projections of the grain. This enables three-dimensional reconstruction of the grain shape by means of a three-dimensional simultaneous iterative reconstruction technique. The complete procedure is described in detail by Ludwig, Reischig *et al.* (2009) and Reischig *et al.* (2013).

For the far-field data, the *ImageD11* software was used. This is part of *FABLE* (http://sourceforge.net/projects/fable/), an open-source software package complete with a graphical user interface, with options for the use of parallel computing; documentation and a developers' corner are also available.

ImageD11 indexes grain orientations from diffraction spots by first assigning spots to powder *hkl* rings for the known unit cell. The scattering vectors between pairs of spots in selected rings are then compared with those that are expected on the basis of the unit cell and *hkl* indices for the rings. When a pair of spots with a consistent angle between them is located, they are used to compute an orientation matrix, and this matrix is used to compute *hkl* indices for all observed scattering vectors. A large number of trial orientation matrices are produced in this way, and those that are retained are selected according to the number of spots that are found to have integer *hkl* values within a tolerance value. A large number of spots found with integer *hkl* values is assumed to indicate a correct orientation. These matrices are later refined, together with the grain positions, after all grains have been located and each peak has

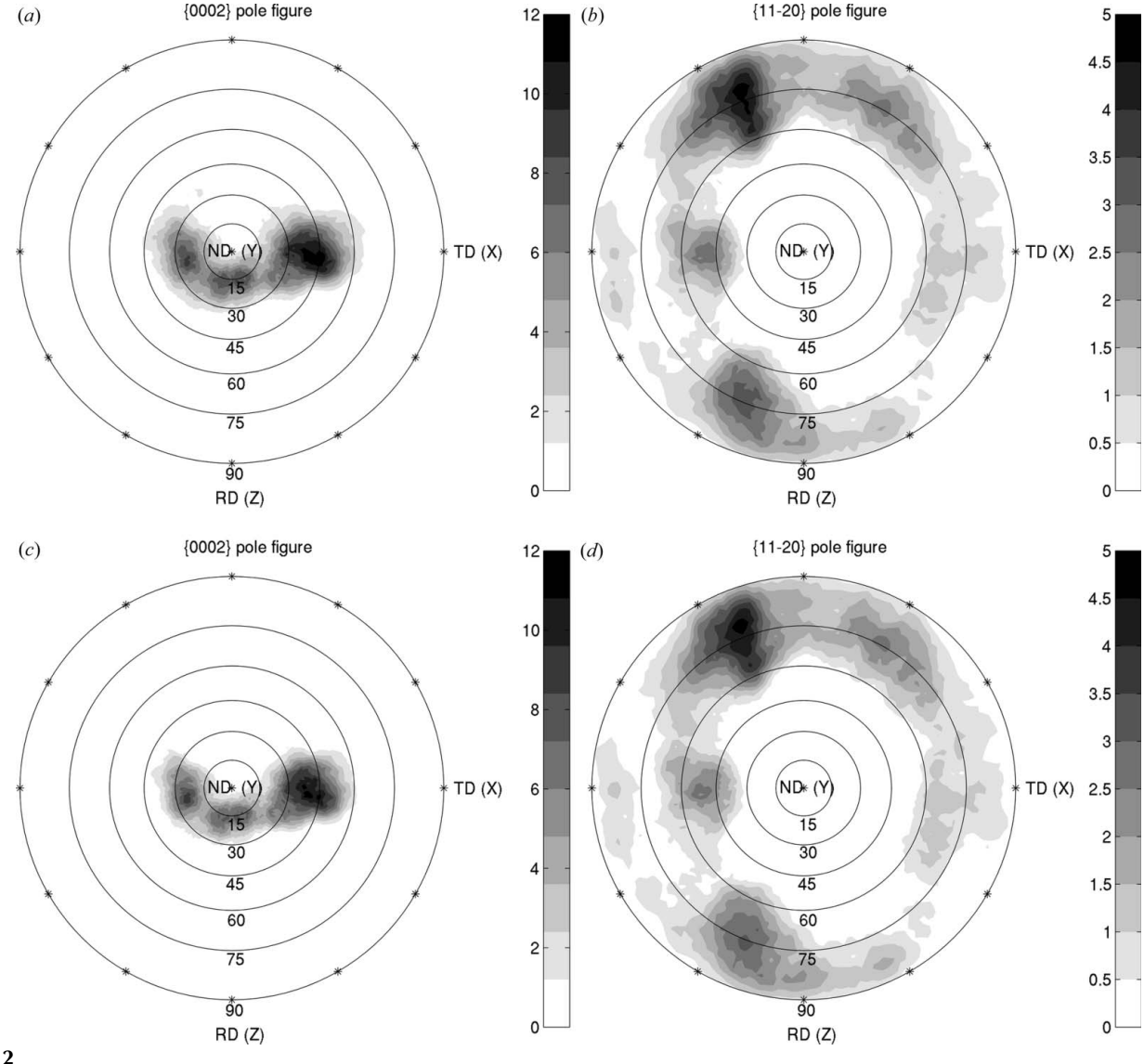

Figure 2
Texture analysis of the data, presented by calculating pole figures. On the top line, they are computed from the near-field data, (*a*) {0002} pole figure and (*b*) {11$\bar{2}$0} pole figure. On the bottom line, the pole figures are computed from the far-field data, (*c*) {0002} and (*d*) {11$\bar{2}$0}. The sample reference system is indicated by the rolling direction (RD), the transverse direction (TD) and the normal direction (ND), which are parallel to the sample *z*, *x* and *y* axes, respectively. The angles ψ and φ describe the pole figure. ψ is the angle between the pole and the ND direction, and it goes from 0 to 90°. φ is the rotation around ND, starting from the positive RD direction to the pole for a right-handed rotation; it goes from 0 to 360°. Rings are drawn for ψ values from 15 to 90°.

been assigned to the grain that gives the best fit (rather than the first grain found).

The choice of tolerance parameters for assigning spots to *hkl* rings, and whether or not to accept *hkl* indices as 'close enough' to being integers, depends on the precision of the experimental data and the density of peaks in the data. The tolerance should be large enough to accept a correct peak, but small enough to reject peaks that are just coincidentally close to expected positions. If the tolerance is too large or the number of peaks is too low then the algorithm can produce false orientations, but this is usually obvious provided some grains are indexed correctly, as the true orientations should fit many more peaks with smaller errors. When the sample size is large in comparison with the detector pixel size and the number of grains is also large, then the peak shifts due to the unknown grain positions are enough to mix up completely which peak belongs to which grain. The software overcomes this problem by assuming a particular position inside the sample prior to computing scattering vectors *etc.*, and using a tolerance value that is as small as would be expected for a point-like sample. To map out the volume of the sample, an algorithm simply loops over a three-dimensional grid inside the sample volume, assuming a point-like sample from each point. The number of peaks, the tolerance values and the grid step are all chosen by the user to best match their experimental conditions.

In this work, grains were accepted if they indexed at least 18 out of 100 spots on the detector on average, and an *hkl* tolerance of 0.02 was used.

The software packages used to analyse the two data sets are both open source and are available to visiting users at the ESRF on beamline ID11. For the case of materials with a small intragranular orientation spread and limited texture, both programs are able to index several thousands of grains in a single data set. The limitation on the number of grains is given by the requirement to locate well separated diffraction spot positions on the two-dimensional detector. The electro-discharge machining process often produces a 're-cast' layer at the sample surface. In this analysis we observed a distinct population of 're-cast' grains close to the surface layer. It is

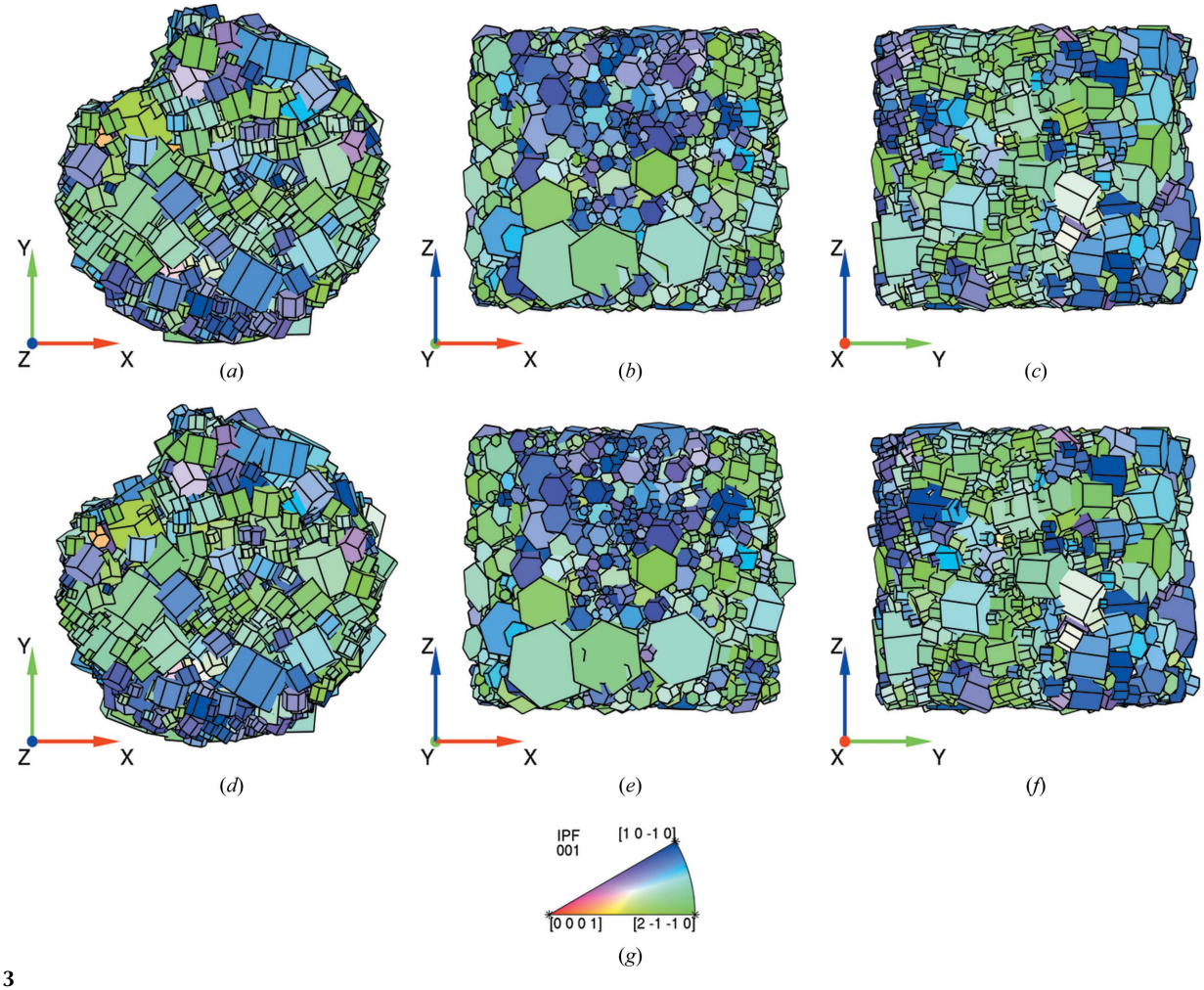

Figure 3
Representations of the grains using hexagonal unit cells. Each unit cell is defined by the corresponding grain centre and scaled according to its size (calculated from the average intensity of diffraction spots assigned to a grain). Parts (*a*), (*b*) and (*c*) are relative to the near-field data, and (*d*), (*e*) and (*f*) are relative to the far-field data. Three projections are shown: (*a*) and (*d*) *xy* plane, (*b*) and (*e*) *xz* plane, (*c*) and (*f*) *yz* plane. (*g*) Orientation colour coding given by the inverse pole figure relative to the sample *z* axis (IPF-Z).

possible that the machining process has deformed some grains intersecting the surface, with the result that they are harder to index and have increased errors.

A number of alternative software packages for indexing grains from far-field diffraction data exist (Lauridsen *et al.*, 2001; Schmidt, 2005, 2014; Moscicki *et al.*, 2009; Bernier *et al.*, 2011; Sørensen *et al.*, 2012; Sharma *et al.*, 2012). Fitting modules like *FitAllB* (Oddershede *et al.*, 2010) also perform a 12-parameter fit for each grain of the centre-of-mass grain positions, orientations and elastic strain tensors, including error estimation and outlier rejection. This may be of interest for future strain analysis on the same material, with particular attention to the characterization of the grain resolved stresses.

3. Comparison of results

The two data sets were analysed using the respective software packages (*DCT* and *ImageD11*). In both cases, around 1750 grains were identified, and their position, size and crystallographic orientation calculated. In the case of *DCT*, the three-dimensional grain shapes were also reconstructed. The following sections report specific details of the indexing results accessible with both methods.

3.1. Crystallographic texture

The grain indexing results were used to plot pole figures in order to represent the crystallographic texture of the sample, as shown in Fig. 2. The {0002} and {11$\bar{2}$0} pole figures are chosen to represent the texture of this material. The density is calculated by considering poles within a radius of 0.1 radians (5.73°) of a given direction, which acts as a smoothing parameter.

3.2. Grain unit-cell representation

A second qualitative way of comparing indexing results on a grain-by-grain basis is shown in Fig. 3, where all the indexed grains are represented as hexagonal prisms, enabling easy identification of the crystal orientation. The differences between the two results are small but detectable to the human eye. Looking carefully at the top and bottom surfaces, one may notice a few missing grains or small differences in grain size and position.

For completeness, a spatially resolved grain map of all the grains, reconstructed from the near-field data, is shown in Fig. 4. In this figure, the asymmetric shape of the sample (a result of the electro-discharge machining), which can be confirmed by absorption tomography, is very clear.

The next sections in the paper analyse these differences and similarities in depth, comparing the distribution of grain size, position and orientation of the same grains found in both data sets.

3.3. Comparison of indexing results and grain-size calculation

Firstly, a comparison of the two techniques regarding the number of indexed grains revealed 1755 and 1743 for the near- and far-field data, respectively. For the grain-size calculation, we assume proportionality between the grain volume ($V_{\rm grain}$) and the average integrated intensity (Int) determined from all diffraction spots that have been assigned to this grain. With this assumption, an estimate of absolute grain volume ($V_{\rm grain}$) can be calculated using equation (1), where $\sum$Int stands for the sum of the average intensities of all indexed grains and $V_{\rm sample}$ corresponds to the illuminated sample volume:

$$V_{\rm grain} = \frac{\rm Int}{\sum \rm Int} V_{\rm sample}. \quad (1)$$

An absolute measure of the illuminated sample volume ($V_{\rm sample}$ = 0.209 mm^3) was obtained from the tomographic reconstruction of the transmission images recorded during the near-field scan.

In order to define an equivalent grain size ($S = 2r$; r is the grain radius), the grain volume ($V_{\rm grain}$) was approximated using a hexagonal prism as the shape and setting the h/r (h is the grain height) ratio to the c/a ratio for pure titanium (1.5857), as expressed in equation (2):

$$V_{\rm grain} = \frac{3}{2} 3^{1/2} \left(\frac{h}{r}\right) r^3, \quad S = 2r. \quad (2)$$

Note that diffraction spots from a grain typically show a spread of intensities, caused by (i) differences in diffraction conditions (*i.e.* structure factor and Lorentz factor), (ii)

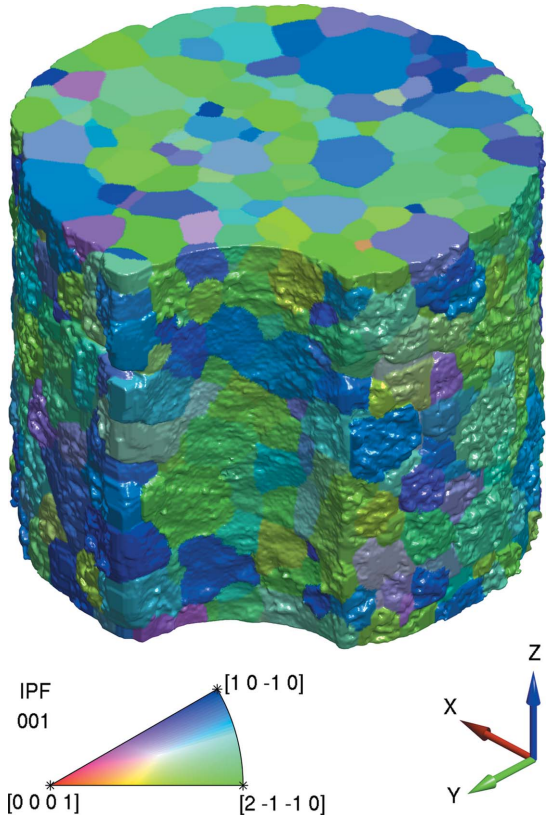

Figure 4
Grain map of the reconstructed sample volume from the near-field data using *DCT*. The grains are coloured according to the IPF-Z map. The represented volume is about half of the real sample volume.

attenuation of the incoming and diffracted beam within the sample (absorption, extinction), and (iii) spatial and temporal inhomogeneities in the incoming beam profile. These factors will affect the accuracy of the absolute volume estimate obtained with equation (1) but can be expected to yield similar estimates when applied to near- and far-field diffraction data from the same sample. In many practical cases, only the contribution from (i) can be corrected, whereas (ii) and (iii) are unknown or not easily accessible. In order to assess the error related to the simplified volume estimate used in equation (1), a comparison of grain volumes obtained with this approach and volumes calculated from the grain map obtained by tomographic reconstruction (Fig. 4) was carried out. This comparison indicates average volume (size) errors of the order of 10^3 μm^3 (1 μm) for grains close to the average grain size in the sample. Similar volume errors were observed when accounting for structure and Lorentz factors in the calculation of the average intensities (Int). This in turn seems to indicate that contributions from (ii) and (iii) dominate the error in the calculation of the absolute grain volume according to equation (1), at least in the conditions used for this experiment.

Fig. 5 compares the grain size of the indexed grains of the two data sets. The agreement between the measurements of the grain size is almost perfect, suggesting a lognormal distribution of the grain size, described by the following equation:

$$f(S;\mu,\sigma) = \frac{1}{S\sigma(2\pi)^{1/2}}\exp\left\{\frac{-[\ln(S)-\mu]^2}{2\sigma^2}\right\}, \qquad (3)$$

where S is the grain size, and μ and σ are, respectively, the mean and the standard deviation of the corresponding normal distribution. For a more quantitative comparison, a fit was performed using the expected lognormal grain-size distribution (solid lines in Fig. 5), which yields mean values for the two distributions of 51.8 and 48.7 μm, respectively, with standard deviations of 21.7 and 21.3 μm, respectively, for near- and far-field data. Both techniques enabled identification of grains down to around 20 μm. However, the far-field methodology shows a slightly higher frequency at the small end compared with the near-field measurement technique, suggesting that, on average, the far-field technique allows one to index smaller grains than the near-field technique, even though there is no significant difference in the minimum detected grain size under the acquisition conditions used in this study.

Given the higher quantum efficiency of the diffraction detector, the latter result is surprising at first sight – one might have expected a spectrum with tails extending down to the (sub-)micrometre grain size. However, the exposure time of CCD-based diffraction detectors must be adjusted such that only a small fraction of the diffraction spots reach the saturation level, beyond which streaking artefacts ('blooming' of the CCD) reduce the quality of the diffraction images. The intensity per pixel scales with the third power of the grain size for grain dimensions smaller than the detector pixel size and continues to increase linearly for grain dimensions larger than the detector pixel size. In the latter case, the integrated diffraction spot intensity is spread over neighbouring pixels and the contribution received by a single pixel corresponds to a grain sub-volume which scales linearly with the equivalent size of the grain. The ratio DR between the strongest and weakest per pixel intensities that have been extracted from the far-field (ff) data is of the order of $DR_{ff} = 4000$ (limited by the dynamic range achievable in a single CCD exposure), and for

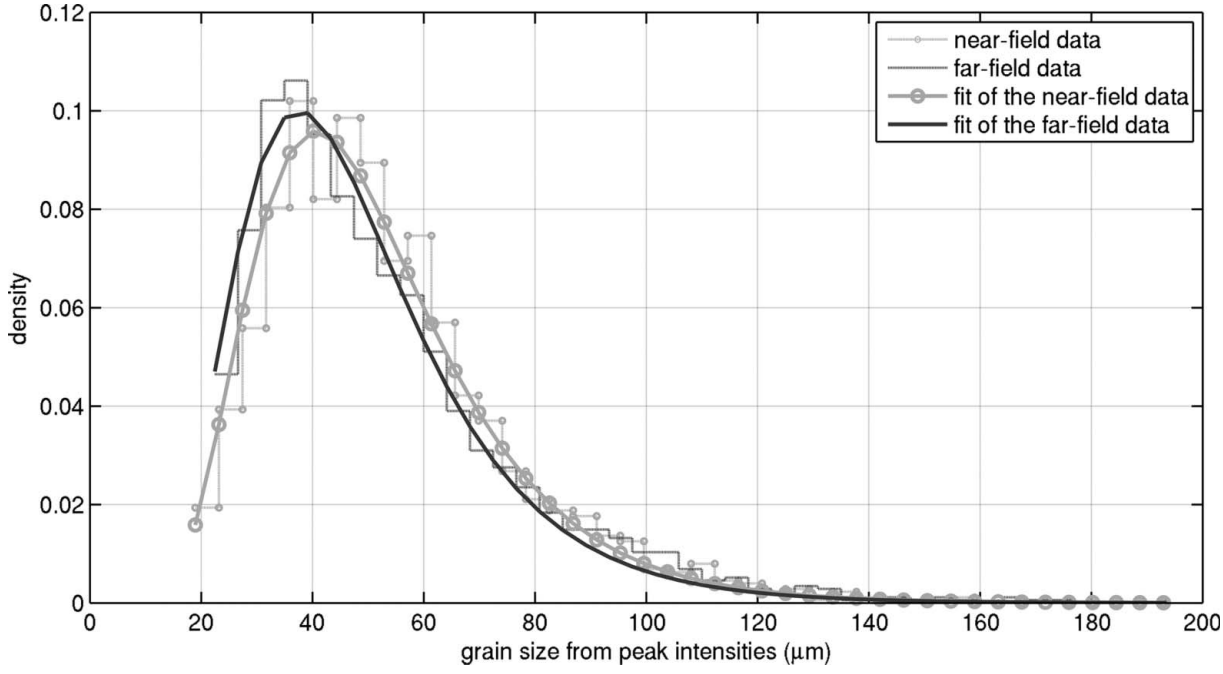

Figure 5
Grain-size distribution shown for both the near- and far-field data (broken lines). The grain-size distribution is fitted with a lognormal distribution (solid lines).

the near-field (nf) detector this ratio is about $DR_{nf} = 30$ (limited by the counting time). Given the different scaling behaviour for the near- and far-field pixel intensities, this results in a similar minimum grain-size detection limit of the order of 10 μm in both cases. We conclude that the grain-size distribution depicted in Fig. 5 is truncated and that smaller grains are present in the sample but could not be detected with the acquisition conditions used in this experiment.

3.4. Matching data sets

The next step in the comparison was to identify to what level the two sets of results agree on individual grains in terms of grain position, size and orientation. In order to match the grains between the two scans, the following criteria were considered: the distance between the centres of mass must be smaller than a factor (DistF) times the actual grain size, the misorientation angle must be smaller than a maximum allowed angle (Angle) and the grain-size ratio must differ by less than a given ratio (Ratio). In summary, the criteria were chosen as

$$\begin{aligned} \text{DistF} &= 0.4, \\ \text{Angle} &= 2.3^\circ, \\ \text{Ratio} &= 2. \end{aligned} \tag{4}$$

Using these tolerances, the number of matched grains is 1465, *i.e.* about 84% of all indexed grains for both techniques were matched. In the following comparison only the matched grains are taken into account, meaning only those grains indexed from *DCT* that can be identified amongst the indexed grains from *ImageD11* and *vice versa*.

3.4.1. Matching data sets: grain position. The first variable studied during this comparison between the matched grains is the position, calculated from the indexing procedure for both techniques. The position of the grains is compared, considering the three components separately as shown in Fig. 6. It is observed that the z component is the most accurate, with a standard deviation of 2.7 μm, whilst the x and y components have larger errors of 6.5 and 6.8 μm, respectively. The larger errors in x and y can be explained as follows. In the current experimental setup (see Fig. 1), the sample z axis is parallel to the rotation axis. Therefore, the grain z position is constant during data acquisition, whereas the x and y positions precess around the z axis, which in turn leads to systematic shifts of the spot positions on the detector. Given the low diffraction angles used in these measurements ($2\theta < 12^\circ$), the vertical shift of the spot position on the detector has a reduced amplitude or sensitivity ($\tan 2\theta \simeq 0.2$), which in turn leads to slightly less accurate position estimates in the xy plane. Furthermore, mechanical imperfections of the rotation stage (wobble and eccentricity) contribute particularly to the error in the xy plane. While it is not possible to compare the absolute errors of the two methods in this way, it can be expected that the near-field detector provides higher positional accuracy and the deviations are mostly due to the larger errors from the far-field data set.

3.4.2. Matching data sets: grain size. The grain sizes determined in the two scans are shown plotted against each other in Fig. 7, considering only the matched grains. One can see that all the grains stay close to the $y = x$ line, indicating good agreement between the measurements. A slight difference in the distribution of the grains in the two parts separated by the diagonal line is visible, especially for grains below an equivalent size of 50 μm. The distribution of these deviations is shown in the top-right histogram, which gives a mean value

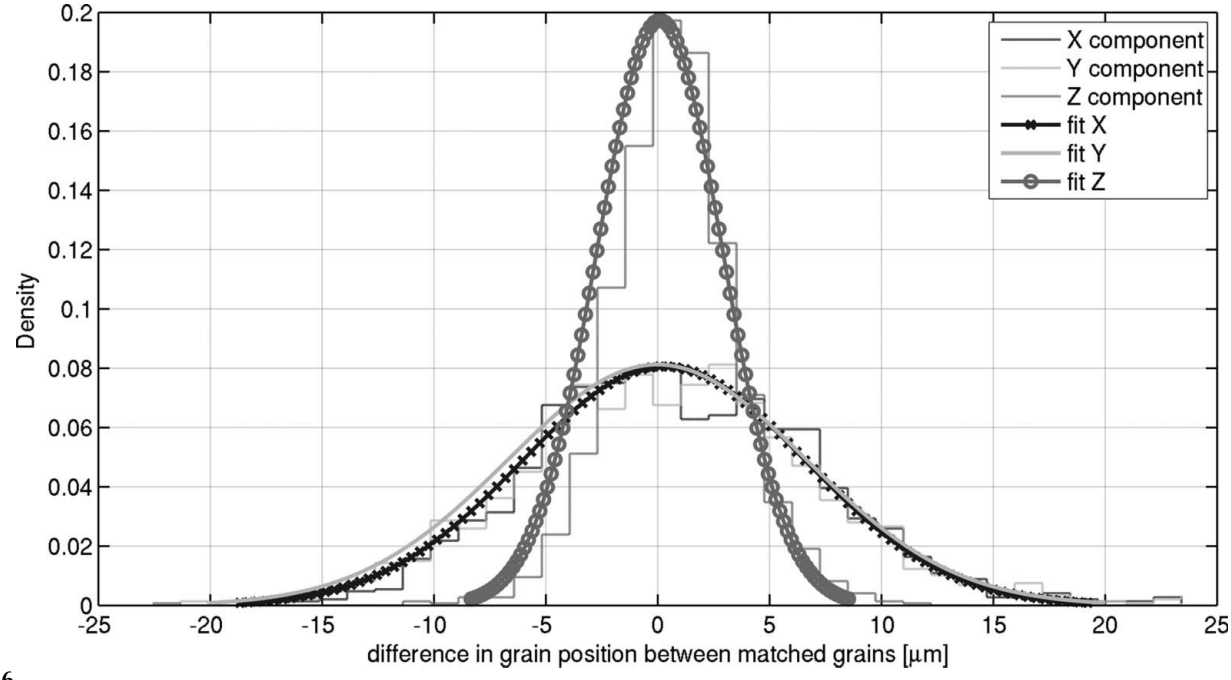

Figure 6
Difference in grain position between near- and far-field data, considering only the matched grains. The total number of points is 1465. The three components are shown with different shading and markers. A normal fit is performed for each component.

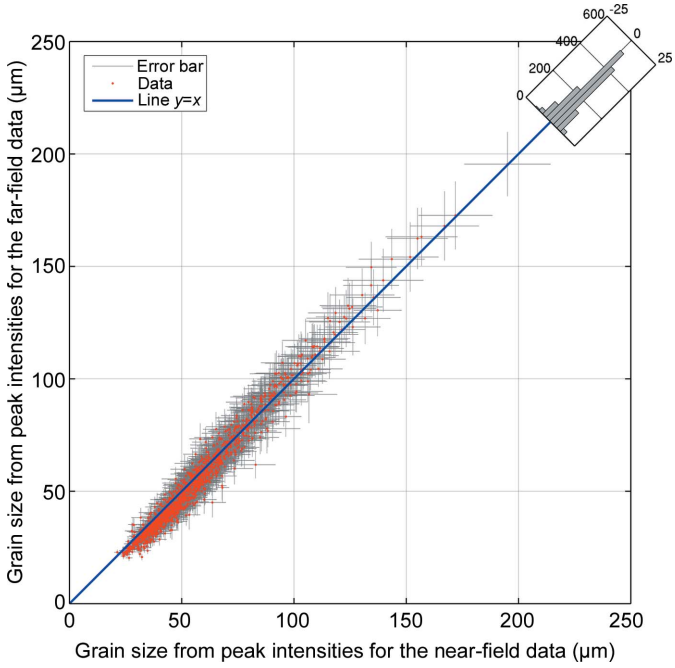

Figure 7
Grain size comparison between near- and far-field data, considering only the matched grains. The total number of points is 1465. The grain size is calculated from the average intensity measured for each grain. The distribution of the deviations from $y = x$ is shown in the top-right histogram.

of 2.9 µm and a standard deviation of 11 µm. The smaller grains appear to be larger in the *DCT* results than in the *ImageD11* results. This difference might arise from differences in the algorithms for measuring the peak intensities. In *DCT*, the peak tail cutoff is scaled by the peak height, while in *ImageD11* the same threshold is used for all spots, so that weak peaks are systematically underestimated.

3.4.3. Matching data sets: grain orientation. The misorientation is the difference in crystallographic orientation between two grains (or crystals), expressed as the smallest rotation between two coordinate systems. One coordinate system can be superimposed on the other by rotating it by an angle around the common axis. Because it is an axis of rotation, the direction is the same in both coordinate systems. Considering the orientation matrix **g**, which can be described by the axis/angle pair (Randle, 1992), one can extract the misorientation angle (θ) and the components of the rotation axis (u, v, w), as explained by Mainprice *et al.* (1993):

$$\theta = \cos^{-1}\left[\frac{1}{2(\mathbf{g}_{11} + \mathbf{g}_{22} + \mathbf{g}_{33} - 1)}\right], \tag{5}$$

$$\begin{aligned} u &= \frac{\mathbf{g}_{23} - \mathbf{g}_{32}}{2\sin\theta}, \\ v &= \frac{\mathbf{g}_{31} - \mathbf{g}_{13}}{2\sin\theta}, \\ w &= \frac{\mathbf{g}_{12} - \mathbf{g}_{21}}{2\sin\theta}. \end{aligned} \tag{6}$$

Fig. 8 presents a histogram of the misorientation for the matched grains, taking the same grain in the two data sets and computing the difference in orientation for each of them. Very close agreement between the measured orientations of the indexed grains for the two data sets can be observed. In this comparison, a misorientation of up to 2.3° is allowed between matched grains. The histogram shows a maximum at around 0.03°, which is of the same order of magnitude as the rotation increment used in the scans (0.05°) and the angular extent of a pixel seen from the sample position (approximately 0.012°).

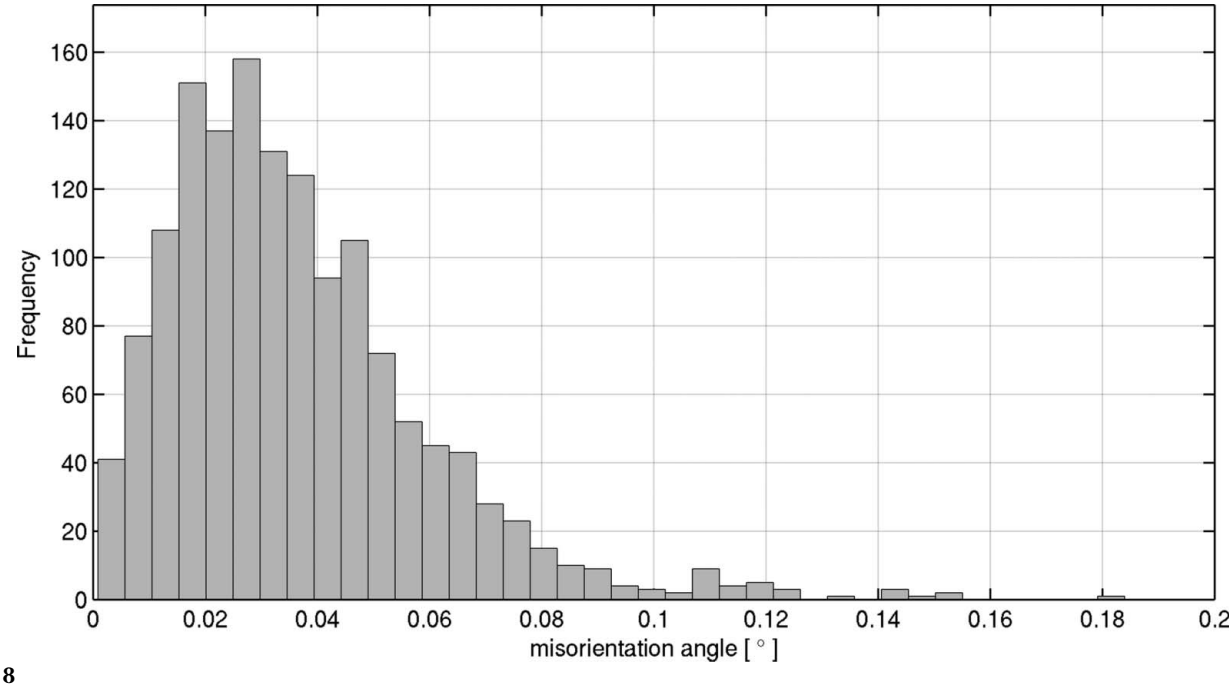

Figure 8
Misorientation angle distribution between near- and far-field data, considering only the matched grains. The total number of points is 1465.

3.4.4. Matching data sets: further analysis. For the current analysis, it was possible to match 1465 grains using a given set of tolerances, which corresponds to 84% of the indexed grains in each data set, leaving about 300 unmatched grains. Adjusting the tolerances can reduce the number of unmatched grains. The analysis presented here suggests that the measurements of grain size and crystallographic orientation are very reliable, and the most significant variations are seen in the calculated grain positions. The far-field detector has a pixel size of 48.5 μm, about 35 times larger than that of the near-field detector (1.4 μm). Consequently, the far-field measurement is not very sensitive to the grain position but instead delivers improved accuracy in the angular measurements of the scattering vectors. In the present analysis the relative distance tolerance was used to match grains, which means that the position of a grain can have an error that is normalized by the actual grain size.

Alternatively, one can consider the absolute distance between two grains (measured in micrometres) as an alternative to the relative distance. Fig. 9 plots the number of matched grains as a function of the tolerance in respect of the relative and absolute distance between grain centres.

One can increase the number of matched grains by changing the criteria, at the risk of introducing false matches or 'multiple' matches, cases in which a grain in one data set can be matched to more than one grain in the other data set. In this analysis, multiple matches are not taken into account and only 'unique' cases are considered: if a multiple match occurs, it is discarded and removed from the list of matched grains. By choosing a relative tolerance of 50% of the actual grain size, more than 1600 grains can be matched and the numbers of unmatched grains are reduced to 91 and 71 for near- and far-field data, respectively. This corresponds to about 0.7% of the sample volume. Note that the analysis already includes grains at the bottom of the gauge volume, which are partially irradiated and where the irradiation may change slightly during the scan because of drifts of the setup, resulting in larger expected errors. The unmatched grains typically populate the lower end of the grain-size distribution. Since these grains are close to the detection limit and represent only a small fraction of the volume, we prefer to take a conservative approach and discard them from the analysis.

4. Discussion

4.1. Differences between the *DCT* and *ImageD11* indexing procedures

The precession of a grain around the rotation axis leads to systematic shifts in the diffraction spot positions recorded on the detector. In order to transform spot positions into scattering vectors, these shifts have to be taken into account in the indexing procedure. In the case of far-field data analysed using *ImageD11*, the problem is solved by dividing the sample into smaller sub-regions (a few times the effective pixel size) and repeating the indexing procedure on the set of scattering vectors computed according to the current position of the subvolume. The actual grain positions and orientation matrices are subsequently refined by means of a Simplex fitting procedure.

In the case of near-field data analysed using the *DCT* code, the transformation from diffraction spot positions into scat-

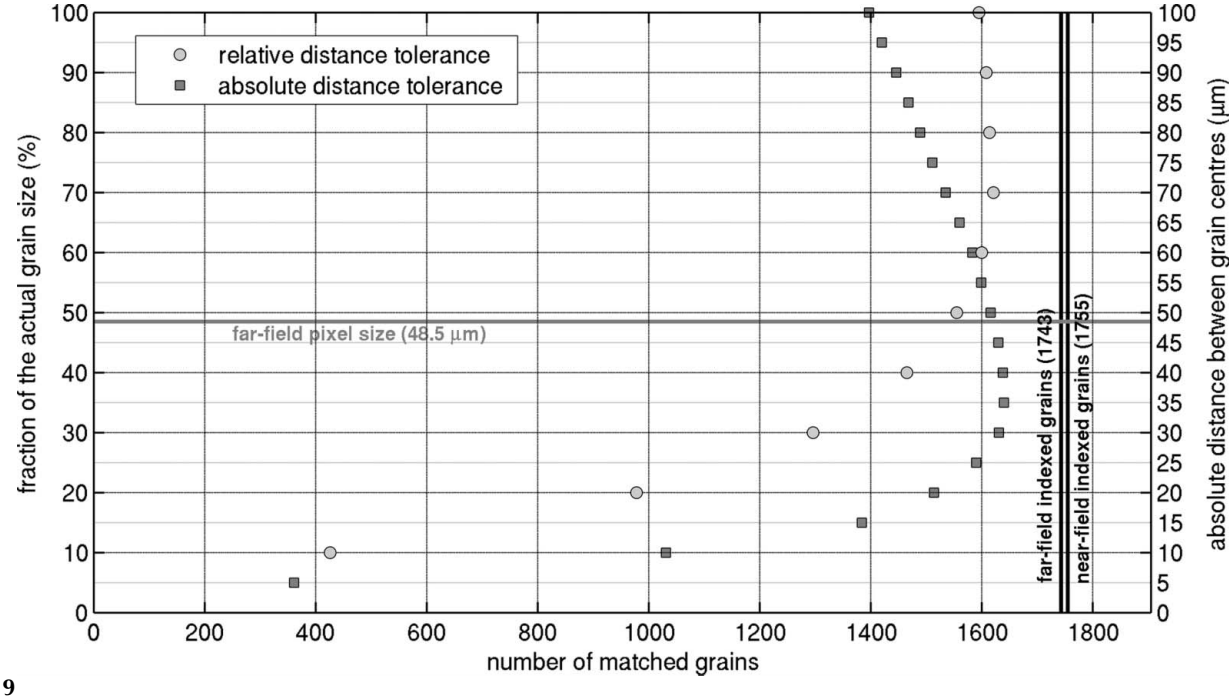

Figure 9
Maximum allowed distance between centres to match grains between near- and far-field data. The absolute distance tolerance goes from 5 to 100 μm (squares). The relative distance tolerance, scaled to the grain size, goes from 0.1 to 1 (circles). The two heavy vertical lines indicate the total number of indexed grains for each data set, while the horizontal grey line indicates the far-field detector pixel size.

tering vectors is based on the concept of Friedel pairs. The positions of the *hkl* and $\overline{hkl}$ reflections observed at a 180° offset in rotation allow for precise determination of the scattering vectors, independent of the grain position (Ludwig, Reischig *et al.*, 2009). The *DCT* indexing procedure uses both spatial (*i.e.* the size of diffraction spot pairs and their distance from the diffraction beam path) and crystallographic (the angle between the scattering vectors) criteria for assigning Friedel pairs of diffraction spots to a given grain. The algorithm performs a combined search, taking these criteria into account simultaneously. The grain position is defined as the point minimizing the distance to the diffracted beam trajectories calculated from the Friedel pairs assigned to the grain. The diffracted beam trajectories are calculated for a Friedel pair from the intensity-weighted centre-of-mass positions of its two diffraction spots.

Since the centre-of-mass positions of sharp diffraction spots on a far-field detector can be determined with higher accuracy, and since sample drifts or mechanical error motions of up to a few micrometres are negligible compared with the pixel size, the accuracy of the scattering vectors determined from far-field diffraction data is in general superior to that obtained from near-field data. As a consequence, the individual grain elastic strain tensors (Oddershede *et al.*, 2010) can be determined with a resolution about one order of magnitude better than that obtained from the near-field diffraction data (Reischig *et al.*, 2013).

As stated earlier, the near-field high-resolution approach allows a three-dimensional reconstruction of the sample volume at the micrometre level, as shown in Fig. 4. One might argue that, with the help of such a voxelized representation, it should be possible to recognize erroneous indexing results (in particular missing grains) by visual inspection of the three-dimensional grain volume. Although this is true for larger grains, previous work on comparison of two-dimensional grain maps produced with DCT and EBSD (Syha *et al.*, 2013) shows that it remains difficult to identify reliably those indexing problems that are related to grains at the lower end of the size spectrum.

Given the large pixel size of the diffraction detector, three-dimensional shape reconstruction of the grains contained in the sample volume is not possible using the far-field diffraction data acquired in this study. However, one could perform a Voronoi or Laguerre tessellation of the three-dimensional volume containing the grain centres, using only the information of grain position and size. Because no grain shape information is available in this case, such a reconstruction can contain significant errors in terms of grain connectivity (neighbours) and grain boundary structure. An assessment of the accuracy of three-dimensional grain shape reconstructions determined from such tessellation procedures is given by Lyckegaard *et al.* (2011).

Both algorithms can index data sets containing up to a few thousand grains, when applied to well recrystallized polycrystalline materials with limited intragranular orientation spread. The presence of grain substructures and texture leads to breakup of diffraction spots. This increases the probability of diffraction spot overlap and will increase the probability of diffraction spot mis-assignment and false indexing. With deformed samples, the increased size of a diffraction spot on the detector leads to a reduction in the number of individual spots that can be resolved and used for indexing.

Alternative approaches exist for indexing near-field diffraction data, particularly if these data have been acquired with a line-focus (one-dimensional) illumination of the sample (Poulsen *et al.*, 2001). Forward-modelling algorithms, such as

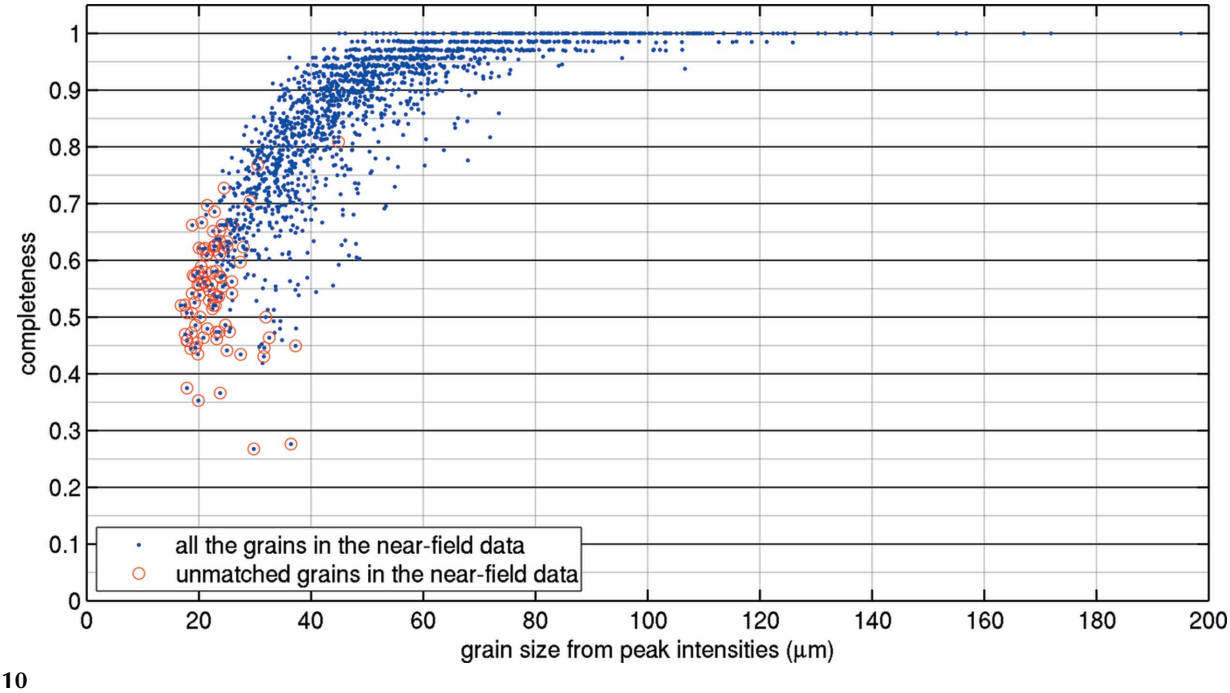

Figure 10
Completeness values for near-field data as a function of grain size. Red circles indicate grains that have not been matched.

those described by Suter *et al.* (2006) and Li & Suter (2013), perform a systematic search over orientation space, and both an orientation and a confidence indicator can be assigned to each voxel in the sample volume. It has been shown that this type of reconstruction algorithm can deal with samples that have undergone significant plastic deformation (West *et al.*, 2009; Li *et al.*, 2012). It would be interesting in the future to compare this class of forward-modelling algorithms with the approaches presented in this paper.

4.2. Unmatched grains

For future users of indexing software for polycrystalline materials, it is important to be aware of limitations and understand the origins of unmatched grains, which have been indexed in only one of the two scans. These may arise because one of the indexing routines fails to detect a real grain or because an algorithm falsely identifies a grain that does not in fact exist. A useful measure of confidence in the indexing of a grain is its completeness. The completeness is the number of indexed reflections from a grain as a fraction of the theoretical number of reflections that should be observed with the given setup. The theoretically expected number of reflections varies slightly between different grains, as it depends on the grain orientation and position. For this prediction, all reflections on the detector are assumed to be detected, even though the weak diffraction signals may be below the detection limit. The average numbers of expected reflections per grain for the near- and far-field acquisition geometries used in this study were about 80 and 150, respectively.

Figs. 10 and 11 plot the completeness as a function of grain size for the near- and far-field data sets, respectively. Unmatched grains are marked with circles in each figure. From Fig. 10 one can state that all the near-field unmatched grains have a grain size lower than 50 µm, while for the far-field unmatched grains (see Fig. 11) there is not such a strong systematic relationship with grain size and completeness. The presence of unmatched grains of a relatively large size and with high completeness in the far-field data suggests either a false indexing result from the *ImageD11* analysis code or that the *DCT* algorithm has failed to find these particular orientations. An alternative scenario is that the matching code has discarded a low-angle grain boundary, where two grains are seen on the far-field detector but only a single grain on the near-field detector.

To understand the remaining discrepancies better, a simulation was carried out to analyse the number of reflections from one data set that could have been assigned to the unmatched missing grains in the other data set. As a first step, the positions of reflections on the far-field detector were computed from the position and orientation of the 91 unmatched grains in the *DCT* data set. A nearby measured peak on the far-field detector was then associated with each simulated reflection, where their distance was within a tolerance limit derived from previous indexing results. Finally, the associated peaks were categorized according to whether or not they had been indexed as a reflection of a grain in the far-field data. The results are shown in Fig. 12 for all the grains, ordered by size.

For a large fraction of these grains, the number of reflections that could be attributed on the far-field detector is below 18, which is the number of reflections on the far-field detector to accept a grain. This may indicate either that they are 'false positives' or that the spot intensities are close to the detection limit of the far-field data set acquired in this study. Moreover, 78.7% of the reflections assigned to the new grains have not been indexed before.

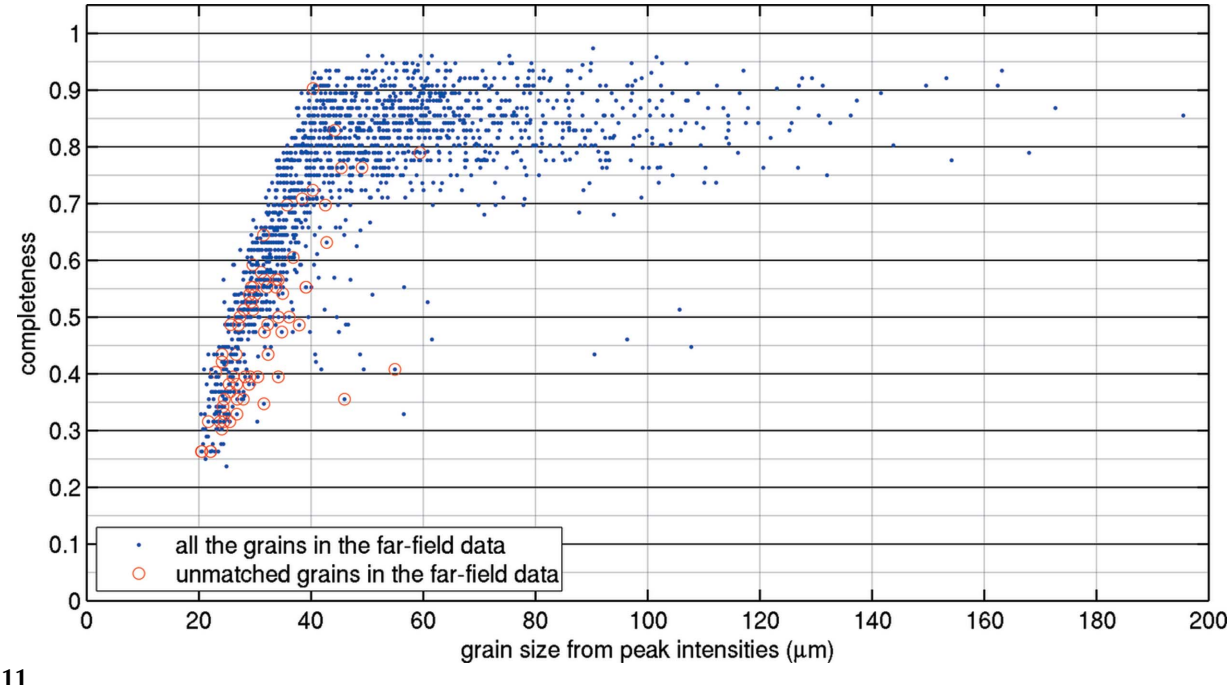

Figure 11
Completeness values for far-field data as a function of grain size. Red circles indicate grains that have not been matched.

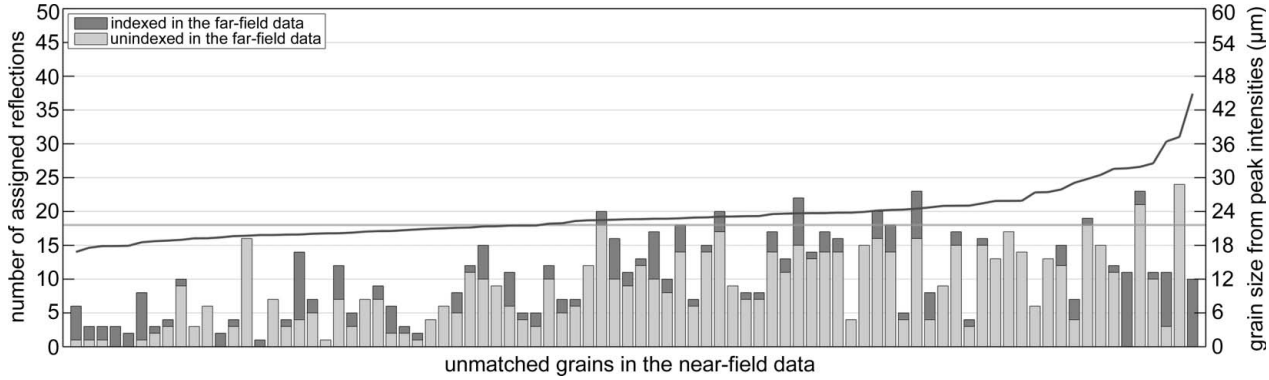

Figure 12
The number of peaks on the far-field detector assigned to the unmatched grains in the near-field data, shown as a bar graph. The peaks are categorized as 'indexed' if they were assigned to a grain in the far-field data, or 'unindexed' otherwise. The number of reflections required on the far-field detector in order to accept a grain is indicated with a light-grey horizontal line. The grains are ordered by grain size, which is plotted as a continuous dark-grey line according to the axis on the right.

The same procedure was repeated by simulating reflections on the near-field detector from the 71 unmatched grains in the far-field data. The results are shown in Fig. 13. The number of assigned reflections on the near-field detector is fairly constant and relatively high, even for the smallest grains. This in turn suggests that the *DCT* code has for some reason failed to index those grains, which are real. Moreover, 98.3% of the reflections assigned to the new grains have not been indexed before.

Observing the results from the forward simulation shown in Figs. 12 and 13, one can draw the conclusion that there are some remaining uncertainties in the indexing procedures for both *DCT* and *ImageD11*. These uncertainties mostly concern small grains and it is difficult to provide objective criteria for the classification of these cases into valid or erroneous indexing results, since, at least for the smaller grains, the low completeness values may be due to insufficient counting statistics.

The methods of indexing presented and discussed in this paper are inverse indexing approaches based on a systematic search through a list of scattering vectors identified by some sort of image segmentation or peak search algorithm. The main advantage of this approach is speed (a few minutes for indexing of up to several thousand grains). However, it is well known that this concept has limitations in the case of strongly textured or plastically deformed materials, since the concept of a grain described by a single orientation will no longer hold and the diffraction spots will start to overlap and break up into sub-peaks, spread out predominantly along the azimuthal direction of the Debye–Scherrer rings.

4.3. Routes for improvement of indexing routines

The indexing procedures discussed in this paper do not include systematic predictable intensity variations of the diffraction signals (*i.e.* structure and Lorentz factors, self-absorption and extinction) assigned to a grain. Adding such an additional constraint could be used for outlier rejection and would help to reduce the number of erroneous spot assignments. This functionality is available in the *FitAllB* code (Oddershede *et al.*, 2012).

Since diffraction spots that have been erroneously assigned to a grain are removed from the list of available spots, the completeness of grains processed at a later stage of the indexing procedure may be deficient. This problem could be alleviated by running the indexing procedure on different

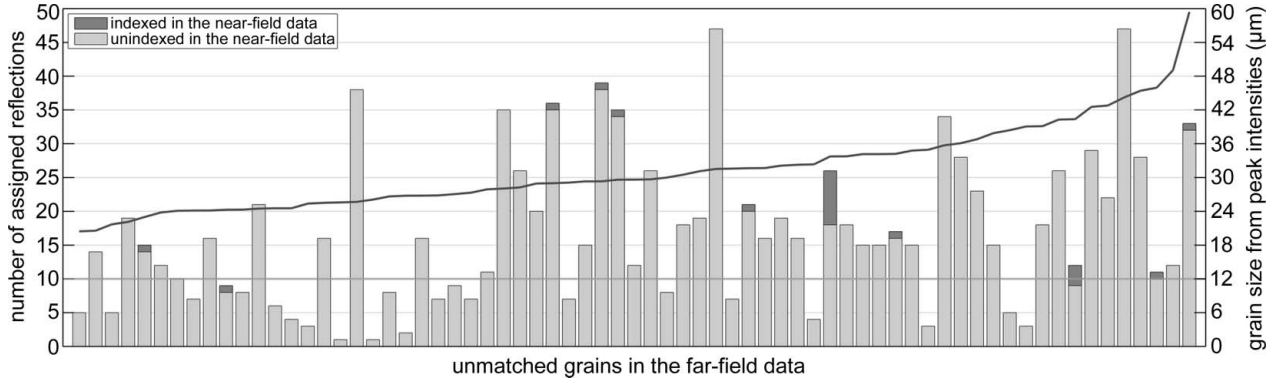

Figure 13
The number of peaks on the near-field detector assigned to the unmatched grains in the far-field data, shown as a bar graph. The peaks are categorized as 'indexed' if they were assigned to a grain in the near-field data, or 'unindexed' otherwise. The number of reflections required on the near-field detector to accept a grain is indicated with a light-grey horizontal line. The grains are ordered by grain size, which is plotted as a continuous dark-grey line according to the axis on the right.

instances of the spot metadata, sorted in a different way. Last but not least, spots assigned to grains with poor quality-of-fit indicators could be kept in the list of spots available for the indexing of new grains. In the case of multiple assignments, these spots would be assigned to the grain yielding the smallest error. This last case is currently under development in the *DCT* code.

Spot overlaps are generally not well accounted for in any procedure where a single spot is matched to a single grain. The centre-of-mass position for the far-field data will be dominated by the stronger signal from the larger grain, which leads to the spot being assigned to that grain. Allowing spots to be assigned to multiple grains and down-weighting them when they overlap would improve the overall accuracy.

5. Conclusions

In the present paper, results are presented for indexing about 1750 grains in a polycrystalline titanium sample. The analysis focuses on the comparison of indexing results obtained with the *DCT* and *ImageD11* software packages, representing near- and far-field techniques, respectively. The measurements of grain position, size and crystallographic orientation are analysed. An important aspect of the analysis is 'matching' (cross-validation of indexing results), whereby the indexed grains from the near-field scan are associated with the respective indexed grains from the far-field scan. The two techniques deliver very similar results in terms of describing a polycrystalline aggregate and there is good, but not perfect, agreement between the results from the two techniques.

The principal difference between the two techniques is the spatial resolution and quantum efficiency of the detector systems employed. Consequently, near-field acquisition schemes are more accurate in spatial resolution and can be used for the reconstruction of spatially resolved grain maps, whereas far-field acquisition schemes are faster and provide more reliable angular resolution for the scattering vectors.

Discrepancies between the two approaches are mainly observed in the lower tail of the grain-size distribution. For the far-field data, the finite dynamic range of the diffraction detector limits the minimum grain size detected with a single exposure in the current study to about 20 μm, whereas for the near-field diffraction data the limitation is rather related to the poor quantum efficiency of the high-resolution imaging system. Both algorithms can be used for fast indexing of data sets containing up to a few thousand grains.

Experimentally, it is possible to carry out these two experiments simultaneously, using the 'three-dimensional' detector concept (Olsen *et al.*, 2009). Here, a high-resolution detector semi-transparent to X-rays is used (in which only a scintillator and 45° mirror are placed in the X-ray beam, with the microscope optics perpendicular), recording the diffraction signal on both detectors at the same time. Simply processing the two data sets independently would allow grain orientation to be transferred between the two programs, leading to a more complete overall picture. An algorithm that matches the diffraction spots across the two data sets prior to indexing should improve the results further, by creating more accurate scattering vectors that are essentially free from errors due to the grain positions in the sample.

The authors are grateful for the help of Sébastien Petitdemange. We further acknowledge Richard Moat (formerly of University of Manchester, UK) for providing the samples and for his assistance during the experiment. The ESRF and its support staff are acknowledged for beam time on beamline ID11. The project was supported financially by the Engineering and Physical Science Research Council in the UK (grant No. EP/F020910/1) and the ESRF.

References

Bernier, J. V., Barton, N. R., Lienert, U. & Miller, M. P. (2011). *J. Strain Anal. Eng. Des.* **46**, 527–547.
Bleuet, P. *et al.* (2009). *Frontiers of Characterization and Metrology For Nanoelectronics: 2009*. AIP Conference Proceedings, Vol. 1173, edited by D. G. Seiler, A. C. Diebold, R. McDonald, C. M. Garner, D. Herr, R. P. Khosla & E. M. Secula, pp. 181–187. College Park: American Institute of Physics.
Coan, P., Peterzol, A., Fiedler, S., Ponchut, C., Labiche, J. C. & Bravin, A. (2006). *J. Synchrotron Rad.* **13**, 260–270.
Holt, J. M. T., Mindlin, H. & Ho, C. Y. (1996). *Structural Alloys Handbook*. West Lafayette: CINDAS/Purdue University.
Labiche, J. C., Mathon, O., Pascarelli, S., Newton, M. A., Ferre, G. G., Curfs, C., Vaughan, G., Homs, A. & Carreiras, D. F. (2007). *Rev. Sci. Instrum.* **78**, 091301.
Larson, B. C., Yang, W., Ice, G. E., Budai, J. D. & Tischler, J. Z. (2002). *Nature*, **415**, 887–890.
Lauridsen, E. M., Schmidt, S., Suter, R. M. & Poulsen, H. F. (2001). *J. Appl. Cryst.* **34**, 744–750.
Li, S. F., Lind, J., Hefferan, C. M., Pokharel, R., Lienert, U., Rollett, A. D. & Suter, R. M. (2012). *J. Appl. Cryst.* **45**, 1098–1108.
Li, S. F. & Suter, R. M. (2013). *J. Appl. Cryst.* **46**, 512–524.
Ludwig, W., King, A., Reischig, P., Herbig, M., Lauridsen, E., Schmidt, S., Proudhon, H., Forest, S., Cloetens, P., du Roscoat, S., Buffiere, J., Marrow, T. & Poulsen, H. (2009). *Mater. Sci. Eng. A*, **524**, 69–76.
Ludwig, W., Reischig, P., King, A., Herbig, M., Lauridsen, E., Johnson, G., Marrow, T. & Buffiere, J. (2009). *Rev. Sci. Instrum.* **80**, 033905.
Lyckegaard, A., Lauridsen, E. M., Ludwig, W., Fonda, R. W. & Poulsen, H. F. (2011). *Adv. Eng. Mater.* **13**, 165–170.
Mainprice, D., Lloyd, G. E. & Casey, M. (1993). *J. Struct. Geol.* **15**, 1169–1187.
Moscicki, M., Kenesei, P., Wright, J., Pinto, H., Lippmann, T., Borbély, A. & Pyzalla, A. (2009). *Mater. Sci. Eng. A*, **524**, 64–68.
Oddershede, J., Camin, B., Schmidt, S., Mikkelsen, L. P., Sørensen, H. O., Lienert, U., Poulsen, H. F. & Reimers, W. (2012). *Acta Mater.* **60**, 3570–3580.
Oddershede, J., Schmidt, S., Poulsen, H. F., Sørensen, H. O., Wright, J. & Reimers, W. (2010). *J. Appl. Cryst.* **43**, 539–549.
Olsen, U. L., Schmidt, S., Poulsen, H. F., Linnros, J., Yun, S. H., Di Michiel, M. & Martin, T. (2009). *Nucl. Instrum. Methods Phys. Res. Sect. A*, **607**, 141–144.
Poulsen, H. F. (2012). *J. Appl. Cryst.* **45**, 1084–1097.
Poulsen, H. F., Nielsen, S. F., Lauridsen, E. M., Schmidt, S., Suter, R. M., Lienert, U., Margulies, L., Lorentzen, T. & Juul Jensen, D. (2001). *J. Appl. Cryst.* **34**, 751–756.
Randle, V. (1992). *Microtexture Determination and Its Applications*. London: Institute of Materials.

Reischig, P., King, A., Nervo, L., Viganó, N., Guilhem, Y., Palenstijn, W. J., Batenburg, K. J., Preuss, M. & Ludwig, W. (2013). *J. Appl. Cryst.* **46**, 297–311.
Schmidt, S. (2005). *GrainSweeper*. http://fable.svn.sourceforge.net/svnroot/fable/GrainSweeper.
Schmidt, S. (2010). *GrainSpotter*. Release 0.82. http://fable.svn.sourceforge.net/svnroot/fable/GrainSpotter.
Schmidt, S. (2014). *J. Appl. Cryst.* **47**, 276–284.
Sharma, H., Huizenga, R. M. & Offerman, S. E. (2012). *J. Appl. Cryst.* **45**, 705–718.
Sørensen, H. O., Schmidt, S., Wright, J. P., Vaughan, G. B. M., Techert, S., Garman, E. F., Oddershede, J., Davaasambuu, J., Paithankar, K. S., Gundlach, C. & Poulsen, H. F. (2012). *Z. Kristallogr.* **227**, 63–78.
Stock, S. R. (2008). *Int. Mater. Rev.* **53**, 129–181.
Suter, R. M., Hennessy, D., Xiao, C. & Lienert, U. (2006). *Rev. Sci. Instrum.* **77**, 123905.
Syha, M., Trenkle, A., Lödermann, B., Graff, A., Ludwig, W., Weygand, D. & Gumbsch, P. (2013). *J. Appl. Cryst.* **46**, 1145–1150.
Vaughan, G. B. M. *et al.* (2010). *Risoe International Symposium on Materials Science. Proceedings*, pp. 457–476. Roskilde: Forskningscenter Risoe Materialeforskning.
Welsch, G., Boyer, R. & Collings, E. W. (1994). *Materials Properties Handbook: Titanium Alloys*, edited by R. Boyer, G. Welsch & E. W. Collings. Materials Park: ASM International.
West, S., Schmidt, S., Sørensen, H., Winther, G., Poulsen, H., Margulies, L., Gundlach, C. & Juul Jensen, D. (2009). *Scr. Mater.* **61**, 875–878.